Electronic Supplementary Material (ESI) for Journal of Materials Chemistry C.
This journal is © The Royal Society of Chemistry 2021

Supporting Information

High-performance short-wave infrared phototransistor based on 2D tellurium/MoS_2 van der Waals heterojunction

Jinrong Yao[a], Fangfang Chen[a], Juanjuan Li[a], Junli Du[b], Di Wu[a], Yongtao Tian[a], Cheng Zhang[c], Jinke Yang[d], Xinjian Li[a,*], Pei Lin[a,*]

[a] *Key Laboratory of Materials Physics of Ministry of Education, School of Physics and Microelectronics, Zhengzhou University, Zhengzhou 450001, People's Republic of China*

[b] *State Grid Henan Electric Power Research Institute, Zhengzhou 450052, People's Republic of China*

[c] *National Joint Engineering Research Center for Abrasion Control and Molding of Metal Materials, School of Materials Science and Engineering, Henan University of Science and Technology, Luoyang 471003, People's Republic of China*

[d] *School of Physical Science and Technology, Southwest Jiaotong University, Chengdu 610031, People's Republic of China*

E-mail: linpei@zzu.edu.cn; lixj@zzu.edu.cn

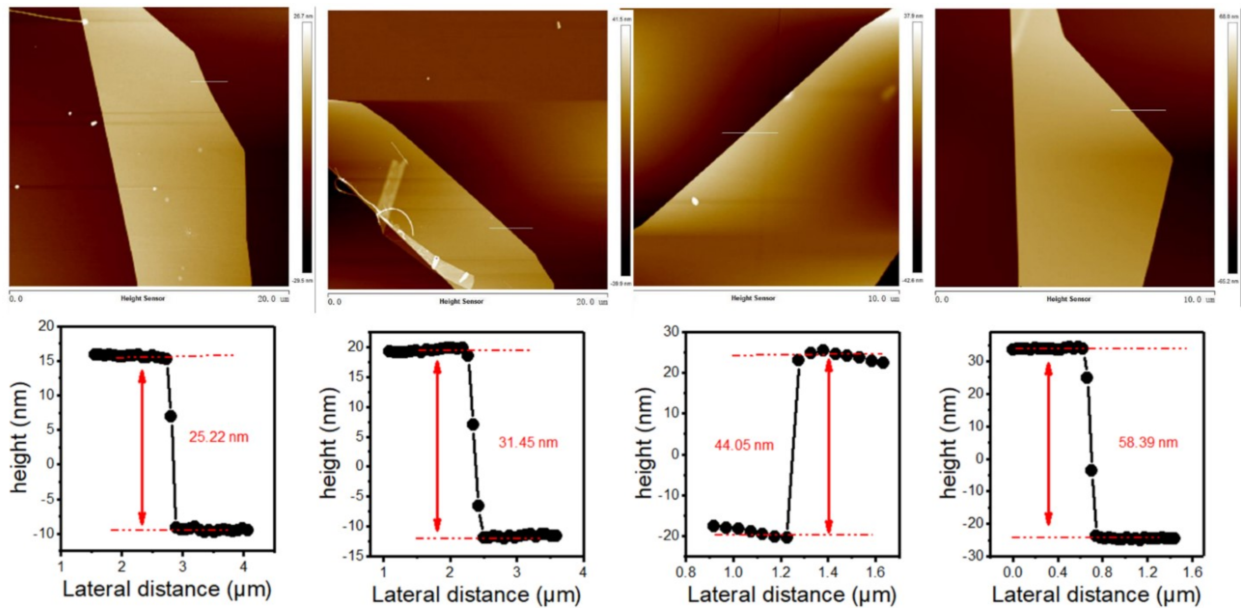

Fig. S1 Atomic force microscope images of the as-synthesized Te nanoflakes, a typical thickness in the range of ~20-60 nm can be observed.

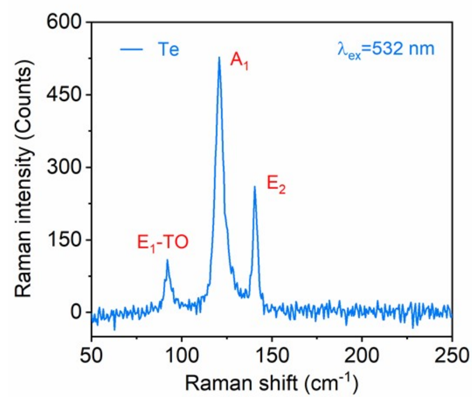

Fig. S2 Raman spectrum of a typical Te flake, the excitation wavelength is 532 nm. Three characteristic Raman-active modes E_1-TO, A_1, and E_2 can be clearly observed.

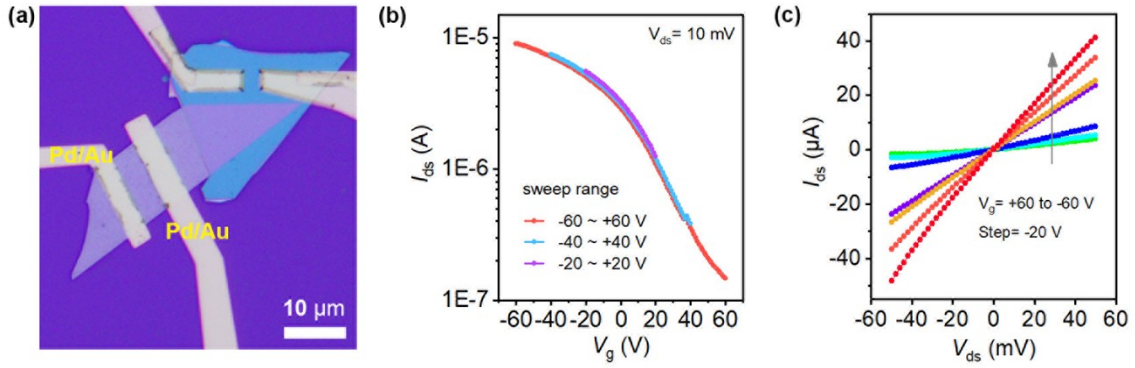

Fig. S3 Electrical characterization of the Te field effect transistor. (a) Optical image of the measured Te transistor, the channel length and width are 4.3 μm and 12 μm, respectively. Thickness of the SiO_2 dielectric layer is 300 nm. The evaporated Pd/Au was used as contact electrode. (b) Transfer curve (I_{ds}-V_g) of the transistor at V_{ds}=10 mV, showing a typical p-type characteristic. (c) Output curves (I_{ds}-V_{ds}) of the transistor under different gate voltages. Field-effect mobility of ~340 $cm^2V^{-1}s^{-1}$ was calculated from the transfer curves by using equation $\mu=[dI_{ds}/dV_g]\times[L/(WC_{oxide}V_{ds})]$, where L/W is the ratio between channel length and width, and C_{oxide} is the capacitance between the channel and the back gate per unit area.

Despite high carrier mobility, the current on/off ratio is typically low ($< 10^3$) due to the large thicknss of as-grown Te flakes. This will lead to a large dark current, which is unfavorable for IR photodetection. Therefore, to suppress the dark current and noise, construction of p-n junction with high gate tunability is still needed for high-performance Te photodetector.

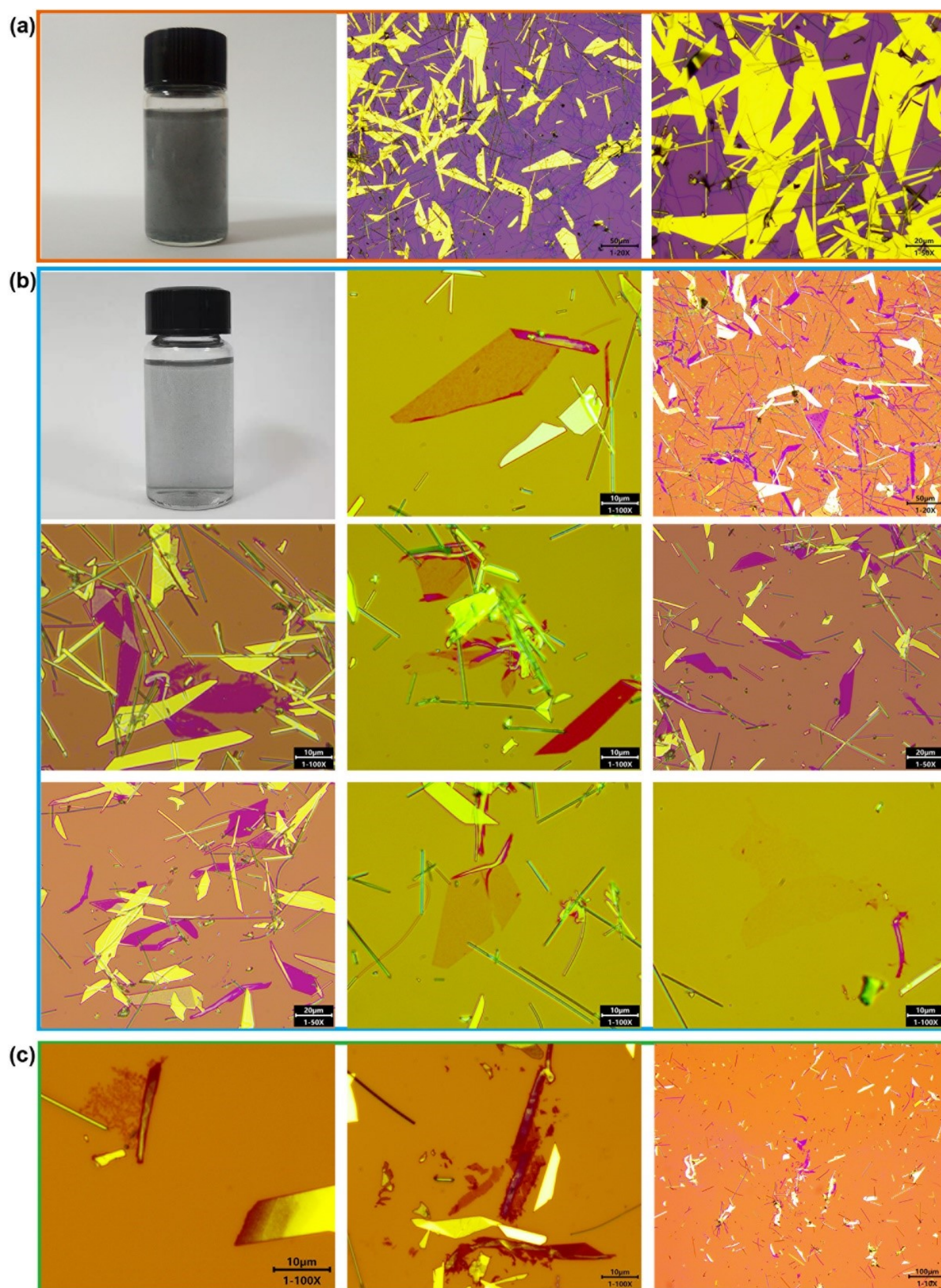

Fig. S4 (a) Optical images of the as-grown Te flakes, which typically show yellow color because of the large material thickness. (b) After storage in DI water (4 °C) for about two weeks, large-scale thin flakes start to emerge and show different colors depending on the thickness. (c) With time further prolonged (about several days), the Te are completely oxidized and dissolved in DI water. Almost no intact ultrathin flakes can be observed.

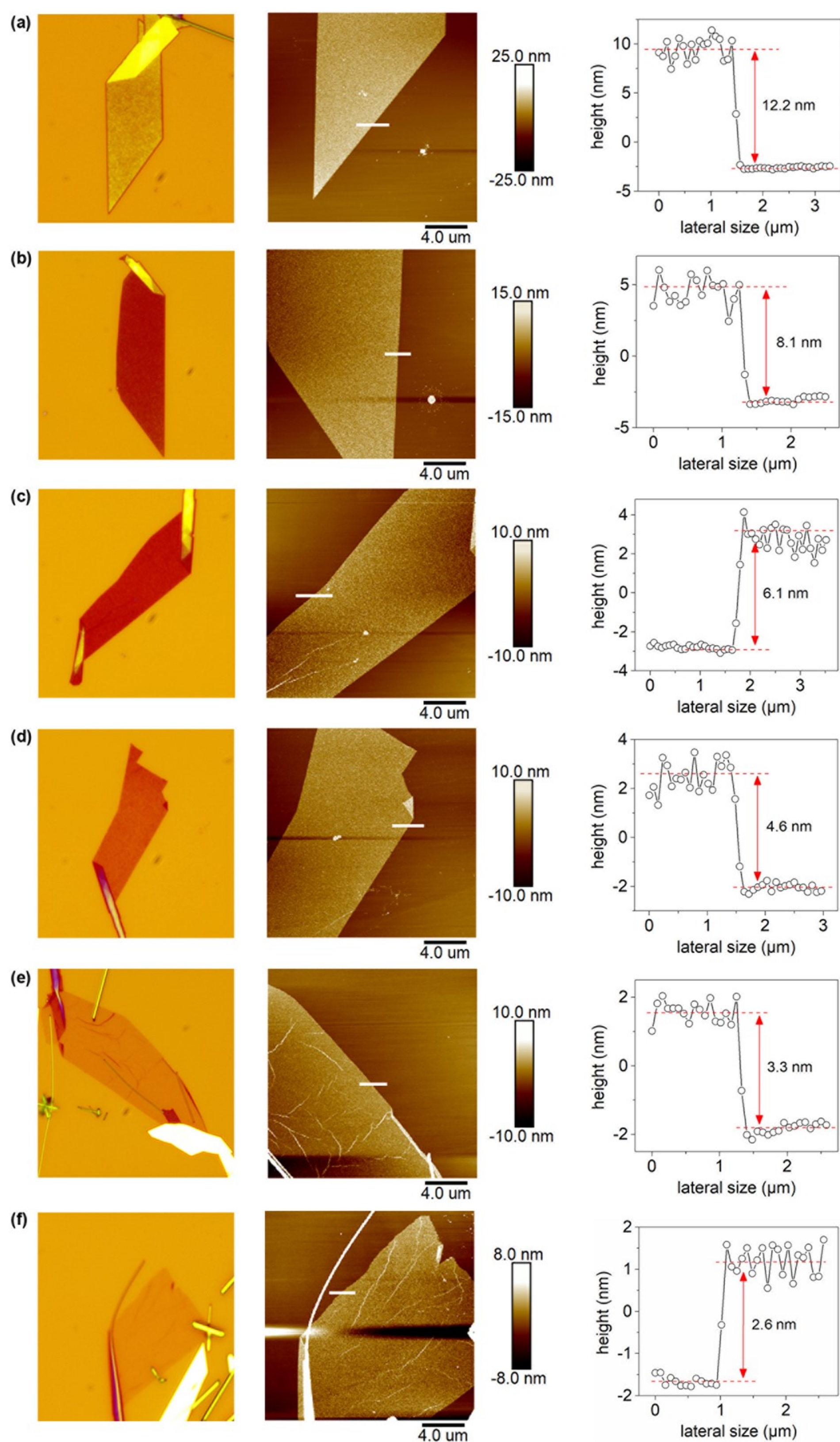

Fig. S5 Optical and atomic force microscope images of thin tellurium. It shows that the Te nanoflakes present different colors depending their thickness, which can be used as a quick guide to estimate the thickness of 2D Te.

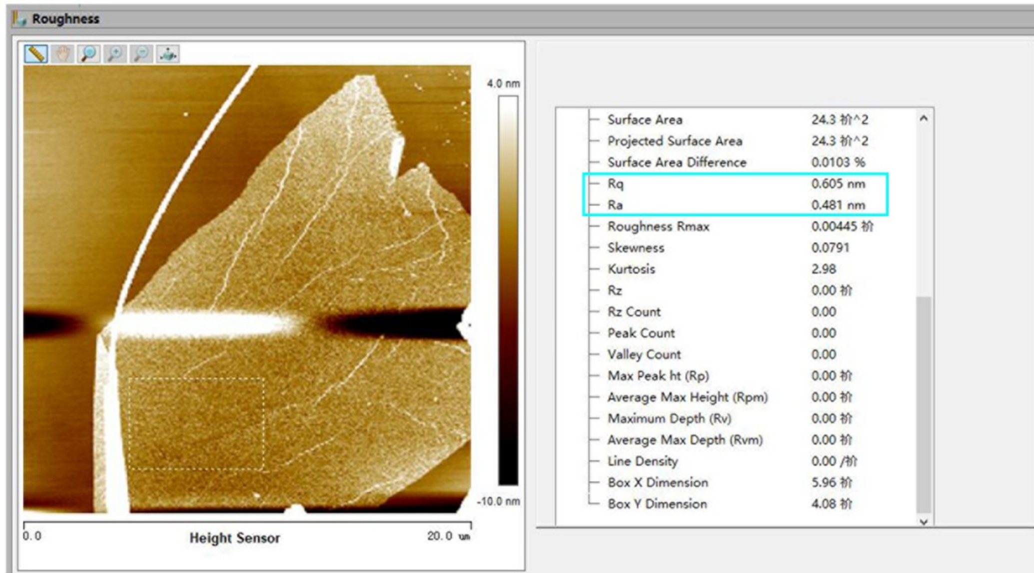

Fig. S6 Evaluation of the surface roughness from AFM image of the Te flake (~2.6 nm thick). The root-of-mean-square (RMS) roughness (Rq) was measured to be ~0.6 nm, and the arithmetic mean roughness (Ra) is only ~0.48 nm.

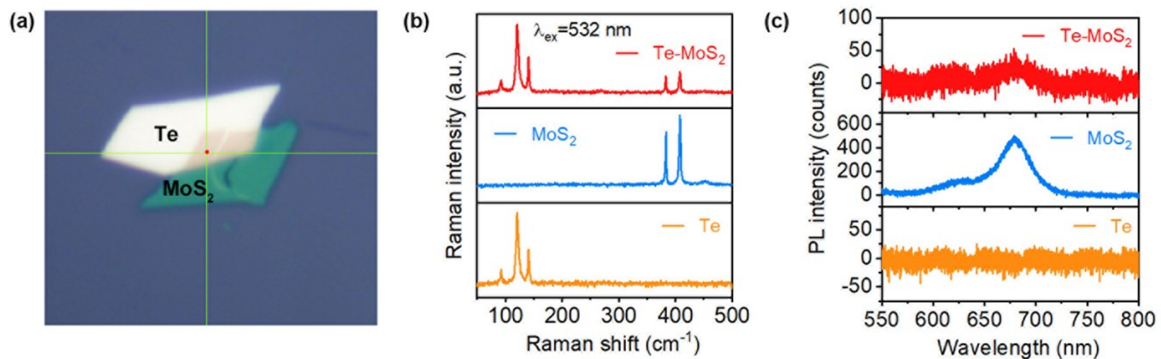

Fig. S7 Raman (b) and photoluminescence (c) characterization of the Te-MoS_2 heterojunction with few-layer MoS_2 on top of Te, the excitation wavelength is 532 nm. Both the characteristic Raman peaks of Te and MoS_2 can be observed from the overlapped area. Compared with individual MoS_2, the PL intensity of MoS_2 measured from the junction area is significantly reduced. As shown in Fig. 4d in the manuscript, a type I heterostructure is formed between Te and MoS_2, and the valence band of MoS_2 is lower than Te. As a result, the photogenerated holes in MoS_2 would transfer to Te instead of

radiatively combining with electrons, resulting in the quenching of MoS_2 PL. This result confirms the effective charge transfer between Te and MoS_2, indicating the formation of high-quality vdW heterojunction.

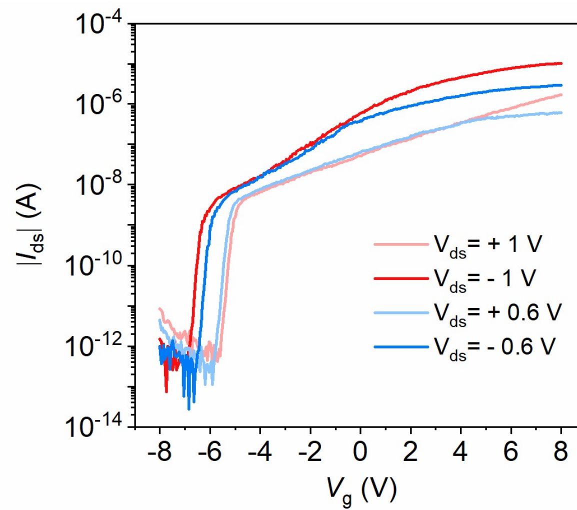

Fig. S8 Transfer curves (I_{ds}-V_g) of the Te/MoS_2 heterojunction FET at positive and negative drain bias, exhibiting typical n-type transport characteristic. As presented in Fig. S3, the Te shows poor gate tunability because of its large thickness. Therefore, the modulation of heterostructure with V_g should be dominated by the bottom, gate-facing MoS_2.

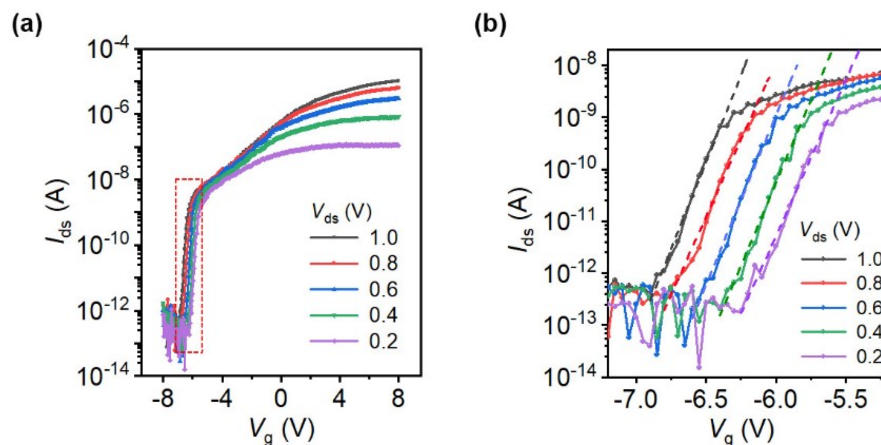

Fig. S9 (a) Transfer curves (I_{ds}-V_g) of the Te/MoS_2 heterojunction at drain voltages of 0.2-1.0 V. (b) The enlarged view of red dashed box shown in (a), which shows a subthreshold swing (SS) of ~150 mVdec^{-1}.

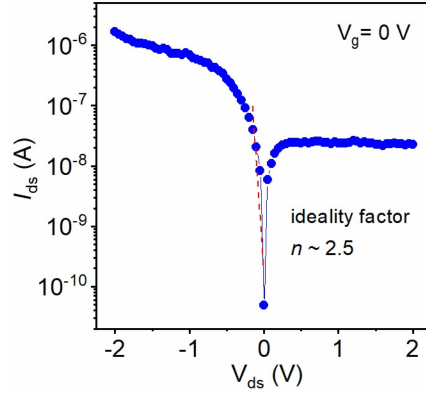

Fig. S10 I_{ds}-V_{ds} curve of the Te/MoS_2 heterojunction at V_g=0 V, from which an ideality factor of ~2.5 could be obtained.

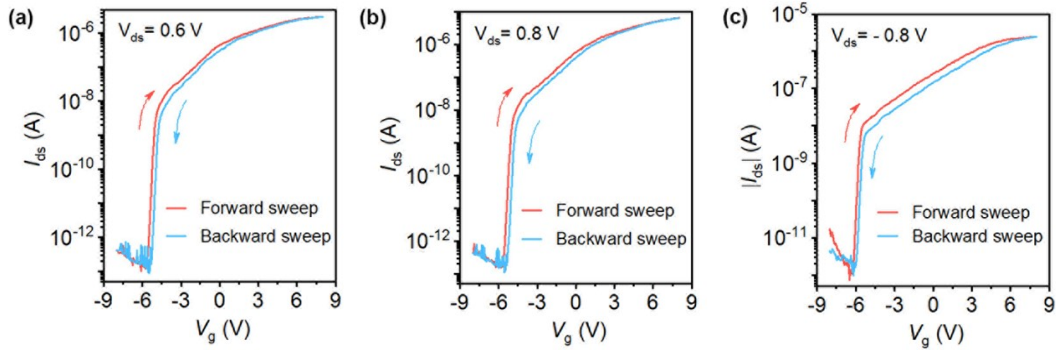

Fig. S11 Hysteretic behavior of the device at fixed drain voltage of 0.6, 0.8, and -0.8 V, demonstrating negligible hysteresis. This can be attributed to the dangling-bond-free surface of h-BN, which reduces the density of trap states.

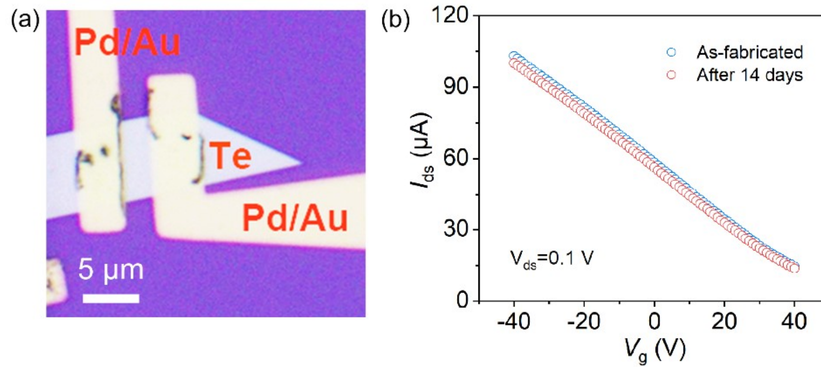

Fig. S12 (a) Optical image of the Te field-effect transistor constructed on SiO_2/Si substrate. (b) Transfer curves of the device, showing negligible change after being exposed in air for 14 days.

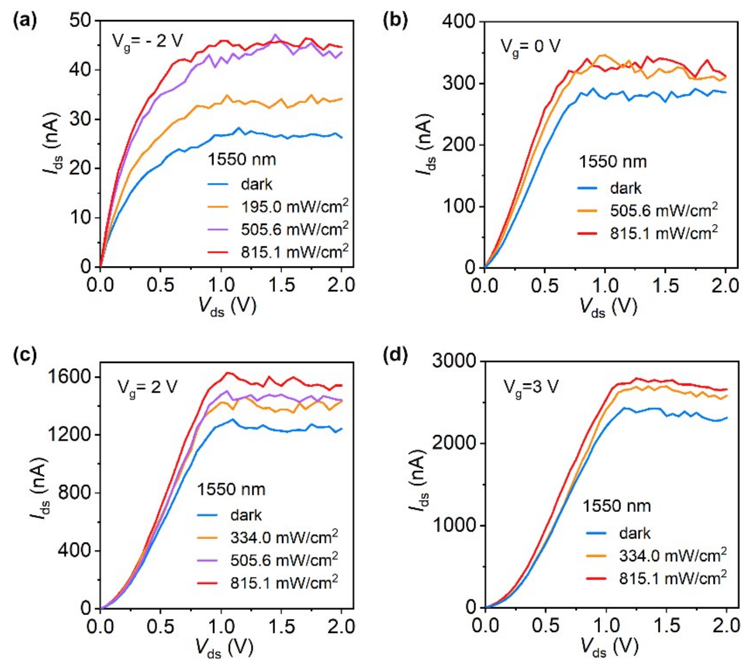

Fig. S13 Photoresponse of output (I_{ds}-V_{ds}) curves of the Te/MoS_2 heterojunction device under different 1550 nm illumination power densities and gate voltages.

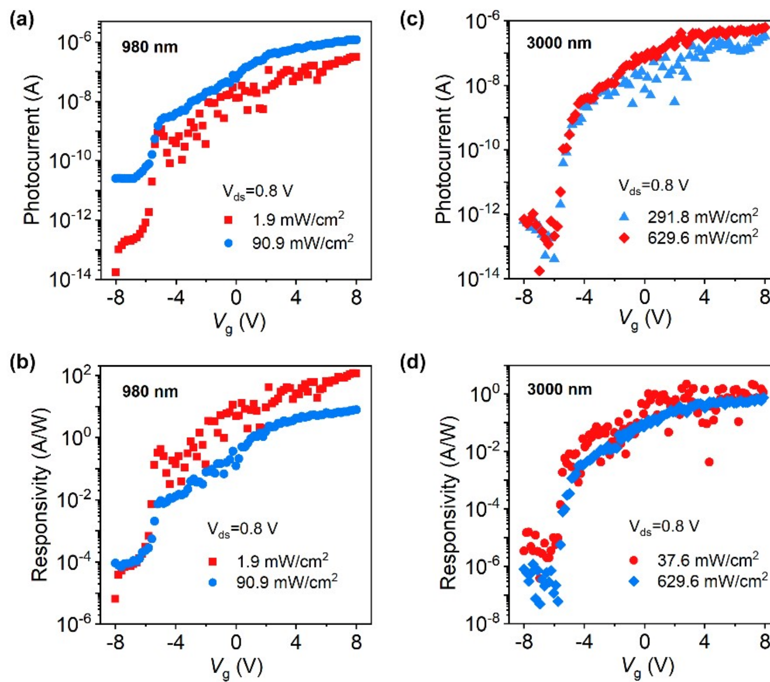

Fig. S14 Calculated net photocurrent (a) and responsivity (b) of the Te/MoS_2 heterojunction at different gate voltages and 980 nm incident laser power densities. The photocurrent (c) and responsivity (d) of the device under different gate voltages and 3000 nm illumination densities.

As mentioned in the manuscript, the net photocurrent was calculated by $I_{ph}=I_{ds}-I_{dark}$, where the I_{ds} and I_{dark} indicate the drain current with and without illumination. The photoresponsivity R is defined as $R=I_{ph}/(P_{in}\times A)$, P_{in} is the power density, A is the effective device area ~138.6 μm^2 (measured from the device's optical image). In the case of an illumination power density (P_{in}) of 12.4 mW/cm^2 (980 nm), the I_{ds} and I_{dark} is 5.31×10^{-6} A and 4.82×10^{-6} A, respectively, yielding a photocurrent I_{ph} of 4.9×10^{-7} A. As a result, the photoresponsivity R is calculated to be ~28.4 A/W. The detectivity is defined as $D=R\cdot A^{1/2}/(2e\cdot I_{dark})^{1/2}$, where R is the responsivity (28.4 A/W), A is the effective area (~138.6 μm^2), e is the electronic charge (1.602×10^{-19} C), and I_{dark} is the dark current (4.82×10^{-6} A). Accordingly, a detectivity of 2.7×10^{10} Jones could be achieved.

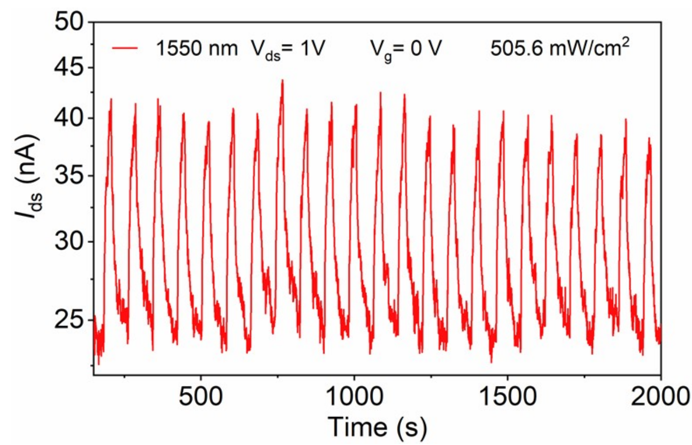

Fig. S15 Time-dependent photoresponse of the Te/MoS_2 vdW heterojunction under the switched on/off 1550 nm illumination. The applied drain voltage is 1.0 V and the gate voltage is 0 V.

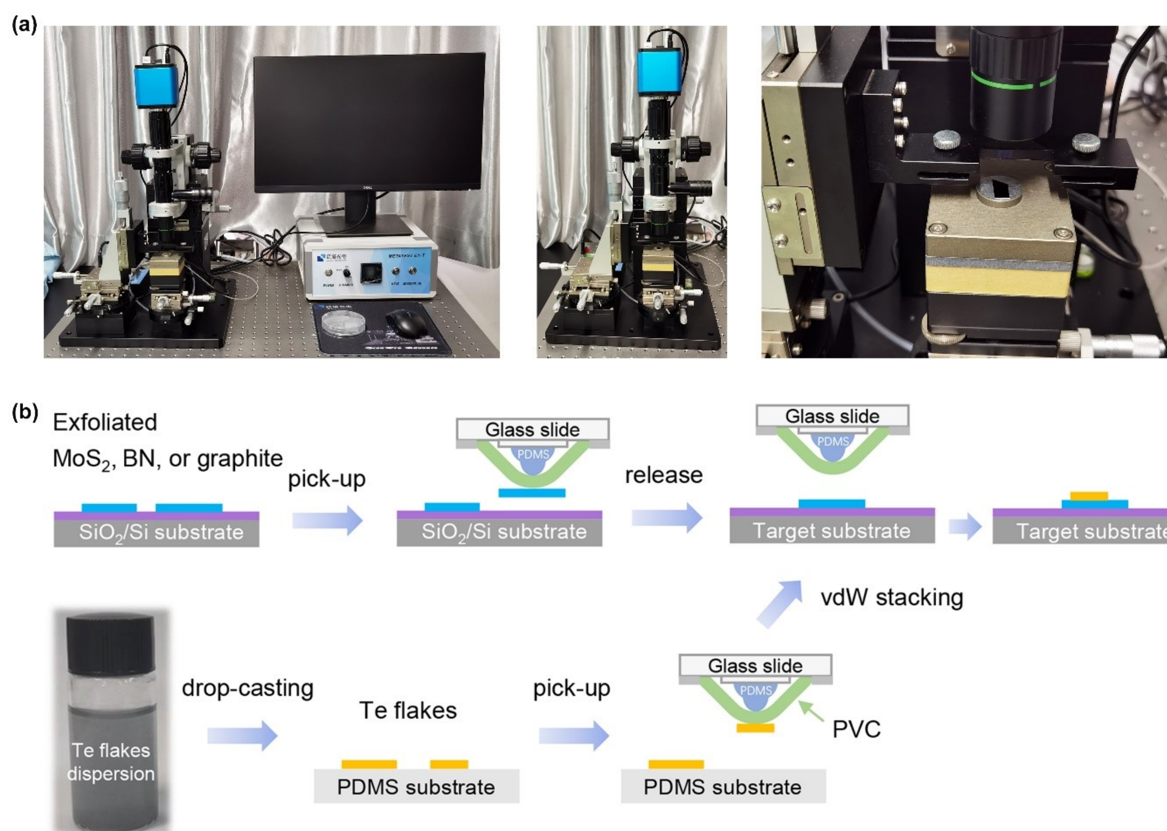

Fig. S16 (a) Optical images of the accurate transfer platform, with which the alignment of materials could be precisely controlled. (b) Schematic representation of the Te/MoS_2/BN/graphite heterostructure stacking procedure following the previous report.[1] The MoS_2 (BN, or graphite) nanosheets were mechanically exfoliated on SiO_2/Si substrate. Then, using a micro-domed PDMS covering poly(vinyl chloride) film (PVC, Reynolds), the material with proper thickness was selectively picked up. Here, the micro-domed PDMS structure was created on the glass slide by sequential dropping and curing of the increasingly small PDMS droplets. Because the adhesion force between PVC and MoS_2 (BN, or graphite) reaches a maximum at ~70 °C, the picking-up procedure was carried out at that temperature. The adhesion force becomes negligible at ~130 °C, allowing materials to be easily released onto the target substrate. However, due to the stronger adhesion force between Te and SiO_2, PVC cannot pick up the Te flakes drop-casted on SiO_2/Si substrate. As a result, the PDMS substrate was used for the Te flakes drop-casting.

Supporting Reference:

1. Y. Wakafuji, R. Moriya, S. Masubuchi, K. Watanabe, T. Taniguchi and T. Machida, *Nano Lett.*, 2020, **20**, 2486-2492.